# Design, Model, and Control of a Dynamic Wireless Power Transfer System for a 30 kW Electric Vehicle Charger Application

Zariff Gomes, Edemar Prado, Yann Le Gall, Gilney Damm, Christophe Ripoll, José Pinheiro

# Design, Model, and Control of a Dynamic Wireless Power Transfer System for a 30 kW Electric Vehicle Charger Application

Zariff M. Gomes, Edemar O. Prado, *member, IEEE*, Yann Le Gall, Gilney Damm, *member, IEEE*, Christophe Ripoll, and José R. Pinheiro, *member, IEEE*

***Abstract*—This paper presents the design, model, and control of a Dynamic Wireless Power Transfer System (DWPT) for a 30 kW electric vehicle charger application. This system allows electric vehicles to receive electric power while running along a road, preserving or even charging its internal battery. The system features primary coils embedded along the road, powered by DC/AC converters connected to a DC bus. The paper presents the system overview and its mathematical model, considering the dynamic behavior of self-inductance and mutual inductance over time. Additionally, a sequencing technique is presented for primary coil selection and activation based on induced current, accounting for motion and misalignment of the secondary coil without relying on the presence of sensors or timing methods. To optimize power delivery, a modified extremum seeking control is designed for autonomously tracking resonance frequency and ensuring soft-switching of power electronic components. This design aligns system components to operate within a predetermined frequency range and power, enhancing overall efficiency. The presented DWPT system is demonstrated through simulations and validated in full-scale experiments using a DS3 Crossback car from Stellantis, recharging the vehicle up to 30 kW under dynamic conditions. Results showcase a maximum efficiency of 90.2% from the DC bus on the primary side to the battery over an 18 m electrical road, highlighting the robustness and effectiveness of the system.**

***Index Terms*—Dynamic wireless power transfer, Electric roads, Inductive power transfer, Modified extremum seeking control, and Power transfer optimization.**

Manuscript received Month xx, 2xxx; revised Month xx, xxxx; accepted Month x, xxxx. This work has received funding from the European Union's Horizon 2020 research and innovation program under Grant Agreement No 875683 (Incit EV project) and from the CNPq (175271/2023-2) and CAPES/PROEX - Finance Code 001.

Zariff M. Gomes, Edemar O. Prado, Yann le Gall and Gilney Damm are with Institut VEDECOM, 23 bis Allée des Marronniers, 78000 Versailles, France. (e-mail: zariff_meira@hotmail.com) (e-mail: yann.legall@vedecom.fr)

Zariff M. Gomes is with the Federal University of Bahia (UFBA), Salvador, 40170-110, BA, Brazil

Gilney Damm is with COSYS-IMSE, Univ. Gustave Eiffel (UGE), IFSTTAR, F-77447, Marne-la-Vallée, France. (e-mail: gilney.damm@univ-eiffel.fr)

Edemar O. Prado are with UFBA, UGE and with the Federal University of Santa Maria (UFSM), Santa Maria, 97105-900, RS, Brazil (e-mail: edemar.prado@ufba.br)

José R. Pinheiro are with UFBA, UFSM and with University of Vale do Itajaí (Univali), Itajaí, 88302-901, SC, Brazil (e-mail: jrenes@gepoc.ufsm.br)

Christophe Ripoll is with Renault SAS, 1 avenue du golf, 78288, Guyancourt, France. (e-mail: chistophe.ripoll@vedecom.fr)

## I. Introduction

Electric Vehicles (EVs) have become a viable alternative for transportation due to their advantages, including the mitigation of environmental issues due to the reduction of carbon emissions during use, decreased fossil fuel dependency, remarkable efficiency, and quieter operation. These EVs are equipped with battery packs that can be charged using onboard battery chargers, which are considered the conventional wired charging technology commercially available [1]–[3].

However, Electric Vehicles have several limitations, particularly the autonomy of the embedded battery: their ability to travel only over limited distances, cost, and long charging time [4], [5]. Multiple factors such as size, weight, cost, logistics, and the recycling process compromise the affordability, carbon consumption, and efficiency of the vehicle [5]–[7].

The current solution to improve the autonomy of EVs is the deployment of fast charging stations at roadside locations and in urban environments. These stations can recharge the battery up to 80% in less than 30 minutes [8], [9]. However, this solution faces operational problems, including congestion at the stations during several periods of the year, electric grid congestion, and the degradation of the State of Health (SoH) of the battery in frequent users [10], [11].

To promote the affordability of EVs, significant improvements are necessary, particularly in terms of cost, size, and battery weight [12], [13]. Currently, the average range of electric cars on the market varies from 150 to 400 km [14], which is considerably less than the range of conventional thermal vehicles, which can travel more than 1000 km [15]. To address this range limitation, different solutions have been proposed in the past, such as increasing battery capacity [16] and increasing power levels to reduce charging time [17]–[20].

Expanding on the challenge of improving the autonomy of EVs, another approach that has been explored is known as Electric Road [1] [21], [22]. Among these approaches, the Dynamic Wireless Power Transfer System (DWPT) is considered one of the most promising options, especially regarding interoperability and security [23]–[25]. These systems enable energy transmission while in motion, providing more autonomy, and reducing battery dependency [26]–[28]. Figure 1

[1]Electric Roads can use Catenary, Conductive Rail, or Dynamic Wireless Power Transfer

shows a description of a DWPT system, where a car receives electric power while running along the road.

In recent years, the development of WPT and DWPT systems for EVs has seen a gradual but significant increase, especially over the past decade [29]–[34]. These systems operate on the fundamental principle of electromagnetic induction, transmitted from successive primary coils on the ground towards a secondary coil embedded into the vehicle. The recent literature focuses on resonant inductive coupling, with the incorporation of a compensation circuit into each induction coil, creating two resonant circuits with a specific resonance frequency [35]–[37].

Talking specifically about DWPT, an important point during operation of these successive coils is the switching on/off strategy among these coils for efficient EV wireless charging. Several solutions have been explored, focusing on different aspects of detection, alignment, and energy transfer. Although some approaches, such as the one proposed by [38], involve the use of additional coils in the primary and secondary couplers for position detection, others such as [39] combine wireless energy transfer with distance detection, minimizing additional hardware. In [40], it uses resonant currents in coils for detection without extra hardware, while [41] introduces an autonomous coil alignment system (ACAS) to address lateral misalignment issues, and [42] proposes a segmented DWPT detection method. Furthermore, [43] presents a cost-effective system that combines a DWPT configuration and extended primary coils. These studies collectively aim to minimize the need for additional hardware while ensuring the robust and cost-effective operation of wireless charging systems for electric vehicles.

In light of the discussion above, this paper begins by presenting a sequencing technique for selecting and activating the primary coil. This approach aims to reduce the system constraints while accounting for the motion and potential misalignment of the secondary part. To ensure proper operation, it is necessary to detect the presence of the vehicle, activate its power supply, and sequence the primary coils accordingly. The initial study enabling vehicle presence detection is introduced in [40] and [44]. This work extends previous research by addressing the management of coil switching on the ground. It ensures the activation of the specific coil aligned with the secondary coil in the vehicle, thus deactivating the other coils on the track.

The paper continues by presenting the overall system model and a modified extremum seeking control. This control strategy leads to the achievement of maximum power delivery by autonomously tracking the resonance frequency and ensuring soft-switching of power electronic components. The remaining sections of the paper are dedicated to testing the proposed system using detailed computer simulations (Matlab Simscape Electrical) and subsequently advancing to full-scale experiments that employ real-size components for the dynamic charging of a *DS3 Crossback* car from *Stellantis*.

The main contributions of this work may be summarized as follows.

- The development of a DWPT system that features continuous and consistent energy transfer.
- The presentation of the overall system and its mathematical model, which takes into consideration the dynamic behavior of self-inductance and mutual inductance with respect to time or speed.
- The development of a sequencing technique for selecting and activating the primary coil based on the induced current, while considering the motion and misalignment of the secondary coil, without relying on a presence sensor or timing methods.
- The design of a modified extremum seeking control for tracking resonance frequency and ensuring soft-switching of power electronic components, achieving maximum power delivery. This design is accomplished by configuring the system components to operate within a predetermined frequency range and power.
- The implementation of the system presented in a real environment, specifically in an urban scenario. This involves recharging a vehicle up to 30 kW in dynamic, semi-dynamic, and static conditions.

## II. Dynamic Wireless Power Transfer System

To characterize the DWPT system, Section II-A provides an introduction to the system, highlighting the fundamental principle of magnetic resonant coupling between the primary coil and the secondary vehicle coil. In Section II-B, the DWPT system under investigation is detailed, with a circuit diagram and operational details. In addition, Section II-C presents the system model.

### A. General Description

The DWPT solution explored in this study is based on the magnetic resonant coupling between the primary coils and the secondary vehicle coil [45]. The power from the utility grid, initially in the form of Alternate Current (AC), is first converted to Direct Current (DC) through the use of an AC/DC rectifier. Then, the obtained DC power is converted further into high-frequency AC power to supply the primary coil. The compensation network reduces the reactive power operating at the resonance frequency [46].

The high-frequency current flowing through the primary coil generates an alternating magnetic field, which in turn induces an AC voltage in the receiving coil. The AC transferred power is then rectified and, through a DC/DC converter, it powers the vehicle's engine and charges the EV battery. The DC/DC converter is also responsible for controlling the power transfer, which allows the vehicle to define the charging power as needed. Figure 1 shows a description of a DWPT system, with the primary and secondary coils. In this work, the control of the power transferred is not addressed, as the system works only at the nominal power. Control strategies for the inductive charging arrangement are presented in [47], [48].

The AC/DC rectifier serves as an active converter, to perform power factor correction in the grid connection. The inverter is a single-phase full-bridge converter driven by classic bipolar modulation. The current-controlled DC/DC converter is bidirectional, allowing for the charging of the intermediate capacitor positioned between the rectifier and the DC/DC

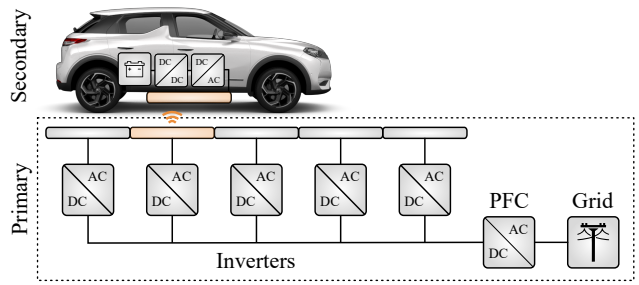


Fig. 1. Overall DWPT Structure.

converter. Pre-charging this capacitor is crucial to prevent overcurrent during the system switch-on. In the charging stage, the DC/DC converter operates as a buck converter to adjust the nominal voltage (typically slightly higher than the battery voltage) along with the current and desired power of the charging system.

The system is free of communication between the primary and secondary sides. The large air gap among the primaries and secondary coils, results in a large leakage inductance for the transformer. To compensate for this significant inductance, series capacitors are introduced on both sides of the transformer. The choice of series compensation simplifies the circuit, avoiding high currents through capacitors found in parallel compensation circuits and eliminating the need for more complex compensation components in the system. However, it is important to note that using series compensation leads to high voltage levels across the inductor and capacitor [49], [50]. This series compensation approach is also applied to the secondary side, maintaining symmetry with the primary side. The dynamic behavior of the system is analyzed in the next sections.

### B. Studied DWPT System

The circuit diagram representing the series-series DWPT system under study is shown in Figure 2.

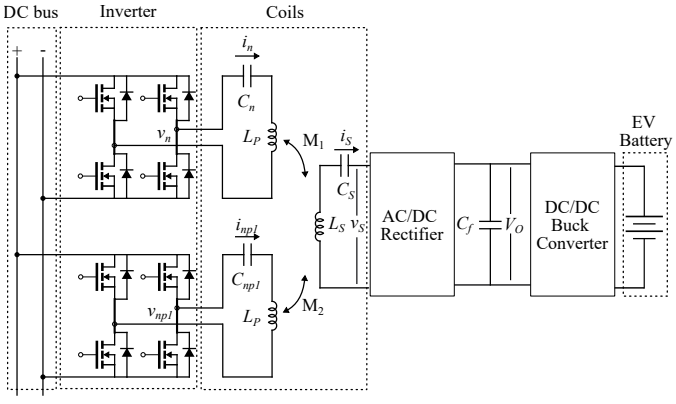


Fig. 2. Equivalent circuit of DWPT system.

The full-bridge converter on the primary side converts the DC voltage ($V_{DC}$) into a full square wave voltage at a switching frequency equal to the resonant frequency of the coupled network. The secondary side converter is a rectifier that converts the secondary AC voltage ($v_s$) to an output DC voltage ($V_O$). $C_f$ is the output filter capacitor, followed by a DC/DC buck converter, which connects to the battery bank. The studied system is designed for a rated power of 30 kW and a rated voltage for the DC bus of 430 V. SiC MOSFETs are considered for system design due to their lower losses in high power levels [51]. The primary and secondary coils are assumed to be identical so that their self-inductance is the same ($L_p = L_s = L$). The resonant tank is designed according to [52], [53]. The values found for $L$ and $C$ are 135 $\mu$H and 33 $n$F, respectively. To simplify the model, the analysis is carried out at the fundamental frequency of the resonant network ($\omega_r$), and the output voltages of the converters are considered perfect sine waves.

### C. System model

A modeling equation for each coil of the system in Figure 2 can be written as:

$$v_n = r_n i_n + v_{C_n} + v_{L_P} \tag{1}$$

where $v_n$ is the applied voltage in the coil, $r_n$ is the self-resistance of the coil wire, $i_n$ is the current in the coil, $v_{C_n}$ is the voltage across the series resonant capacitor and $v_{L_P}$ is the voltage across the inductor.

The equations considering one secondary coil and several primary coils can be represented in matrix form:

$$\hat{V} = \hat{R}\hat{I} + \hat{V}_C + \hat{V}_L \tag{2}$$

where $\hat{V}$ is the vector of the voltages applied or induced in the coils, $\hat{R}$ is the matrix of the resistances, $\hat{I}$ is the vector of the currents flowing in the coils, $\hat{V}_C$ is the vector of the voltages across the resonant capacitors and $\hat{V}_L$, the voltage across the inductors of the coils. These matrices are represented as:

$$\hat{V} = \begin{bmatrix} v_n \\ v_s \\ v_{np1} \\ v_{nm1} \\ v_{np2} \\ \vdots \end{bmatrix}, \hat{I} = \begin{bmatrix} i_n \\ i_s \\ i_{np1} \\ i_{nm1} \\ i_{np2} \\ \vdots \end{bmatrix}$$

$$\hat{V}_C = \begin{bmatrix} v_{C_n} \\ v_{C_s} \\ v_{C_{np1}} \\ v_{C_{nm1}} \\ v_{C_{np2}} \\ \vdots \end{bmatrix}, \hat{V}_L = \begin{bmatrix} v_{L_n} \\ v_{L_s} \\ v_{L_{np1}} \\ v_{L_{nm1}} \\ v_{L_{np2}} \\ \vdots \end{bmatrix}$$

$$\hat{R} = \begin{bmatrix} r_n & 0 & 0 & 0 & 0 & \cdots \\ 0 & r_s & 0 & 0 & 0 & \cdots \\ 0 & 0 & r_{np1} & 0 & 0 & \cdots \\ 0 & 0 & 0 & r_{nm1} & 0 & \cdots \\ 0 & 0 & 0 & 0 & r_{np2} & \cdots \\ \vdots & \vdots & \vdots & \vdots & \vdots & \ddots \end{bmatrix}$$

where the subscript $n$ refers to the primary coil, $s$ to the secondary coil, $np1$ is the primary coil in position $N+1$, $nm1$

is the primary coil in position $N-1$ and $np2$ is the primary coil in position $N+2$. The coil sequence is also discussed in Section III and shown in Figure 4.

The voltage across the capacitors can be represented as:

$$\frac{d}{dt}\hat{V}_C = \hat{C}\hat{I}$$

where $\hat{C}$ is the matrix of capacitors.

$$\hat{C} = \begin{bmatrix} \frac{1}{C_n} & 0 & 0 & 0 & 0 & \cdots \\ 0 & \frac{1}{C_s} & 0 & 0 & 0 & \cdots \\ 0 & 0 & \frac{1}{C_{np1}} & 0 & 0 & \cdots \\ 0 & 0 & 0 & \frac{1}{C_{nm1}} & 0 & \cdots \\ 0 & 0 & 0 & 0 & \frac{1}{C_{np1}} & \cdots \\ \vdots & \vdots & \vdots & \vdots & \vdots & \ddots \end{bmatrix}$$

To determine the voltage across the inductors, it is necessary to define the equation for the total flux linkage. The total flux linkage in coil $n$ is represented as:

$$\begin{aligned}\lambda_n = L_n i_n + M_{n.s} i_s + M_{n.np1} i_{np1} + M_{n.nm1} i_{nm1} \\ + M_{n.np2} i_{np2} + M_{n.nm2} i_{nm2} + ...\end{aligned} \tag{3}$$

where $\lambda_n$ is the total flux passing through the coil $n$, $L_n$ is the self-inductance of the coil $n$, $M_{n.s}$ is the mutual inductance between the coil $n$ and the secondary coil $s$, $M_{n.np1}$ is the mutual inductance between the coil $n$ and its neighbor coil $np1$ and successively.

The equation can be expressed in matrix form:

$$\hat{\Lambda} = \hat{L}\hat{I}$$

where:

$$\hat{L} = \begin{bmatrix} L_n & M_{ns} & M_{n.np1} & M_{n.nm1} & \cdots \\ M_{s.n} & L_s & M_{s.np1} & M_{s.nm1} & \cdots \\ M_{np1.n} & M_{np1.s} & L_{np1} & M_{np1.nm1} & \cdots \\ M_{nm1.n} & M_{nm1.s} & M_{nm1.np1} & L_{nm1} & \cdots \\ \vdots & \vdots & \vdots & \vdots & \ddots \end{bmatrix}$$

The time variation of the flux produces the inductance voltage.

$$\hat{V}_L = \frac{d}{dt}\hat{\Lambda} \tag{4}$$

Replacing (4) into (2) leads to:

$$\begin{aligned}\hat{V} &= \hat{R}\hat{I} + \hat{V}_C + \frac{d}{dt}\left(\hat{L}\hat{I}\right) \\ &= \hat{R}\hat{I} + \hat{V}_C + \frac{d\hat{L}}{dt}\hat{I} + \frac{d\hat{I}}{dt}\hat{L}\end{aligned} \tag{5}$$

The inductance matrix depends on position. The movement of the secondary coil generates variations in the values of self-inductance and mutual inductance for all the coils. Depending on the placement of ferromagnetic material in the secondary and primary coils, this variation can be larger or smaller. For example, when only the secondary coil is made of ferrite, the change in self-inductance is significant on the primary side due to the proximity of a ferromagnetic material around the coil. On the other hand, on the secondary side, self-inductance remains almost unchanged. The size and shape of the coils are additional parameters that can influence the behavior of the variation of the value of the inductances. The influence of this variation is represented in (5) by the term $\frac{d\hat{L}}{dt}\hat{I} + \frac{d\hat{I}}{dt}\hat{L}$.

As a function of position $s$, the matrix can be expressed as:

$$\begin{aligned}\hat{V} &= \hat{R}\hat{I} + \hat{V}_C + \frac{d\hat{L}}{ds}\frac{ds}{dt}\hat{I} + \frac{d\hat{I}}{dt}\hat{L} \\ &= \hat{R}\hat{I} + \hat{V}_C + \frac{d\hat{L}}{ds}\upsilon\hat{I} + \frac{d\hat{I}}{dt}\hat{L}\end{aligned}$$

where $\upsilon$ is the speed of the secondary coil.

This derivation simplifies the characterization of the system since the behavior of the inductances can be known by simulation and measurements. In a symmetric track, the matrix of inductances is symmetric, which reduces and simplifies the model.

## III. Modified Extremum Seeking Control Design

The resonance condition is the main target of the control strategy on the primary side. The resonance ensures Zero Current Switching (ZCS), and Zero Voltage Switching (ZVS), reducing power losses on the inverter.

In a dynamic inductive charging system, the relative position between the primary coil and the secondary coil is constantly changing while the vehicle is moving. It means that mutual inductance and even self-inductance change at all times and depend on the relative distance between the primary and secondary coils and the ground clearance.

Figure 3 shows the variation of the coupling coefficient ($k$) versus the relative distance of the secondary coil of a bench with two coils on the ground and one coil in the vehicle (obtained by ANSYS simulation). The numerical values for the coupling coefficients shown in Figure 3 are presented in Table I.

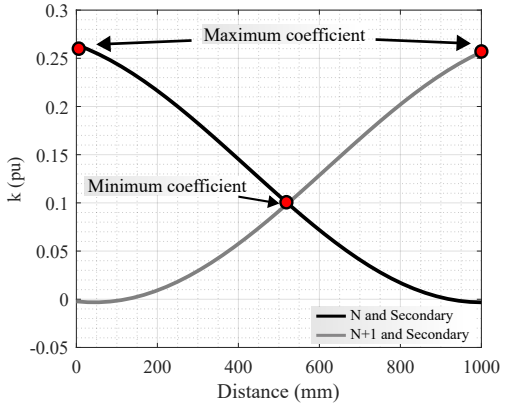


Fig. 3. Coupling coefficient variation.

In the worst-case scenario of misalignment, the coupling coefficient reaches a minimum value of approximately 0.1 (point with coils $N$ and $N+1$ presents equivalent values). At its peak, the coupling coefficient reaches 0.25, which falls within the typical range for wireless charging systems, as reported in the literature (0.1 - 0.3) [54], [55]. This performance indicates that even under significant misalignment conditions,

TABLE I
COUPLING COEFFICIENT AMONG SECONDARY AND PRIMARIES $N$ AND $N+1$.

| Distance (mm) | $k$ ($N$, $S$) | $k$ ($N+1$, $S$) |
|---|---|---|
| 0 | 0.263286398 | -0.010369708 |
| 58 | 0.258012839 | -0.010741348 |
| 174 | 0.224726772 | -0.002419497 |
| 232 | 0.203729683 | 0.008868946 |
| 290 | 0.182808898 | 0.024622141 |
| 348 | 0.162641426 | 0.043145191 |
| 406 | 0.143081066 | 0.062945265 |
| 464 | 0.12384477 | 0.082912017 |
| 522 | 0.104717184 | 0.102744861 |

the system maintains reliable power transfer efficiency, while remaining comparable to existing designs in terms of coupling capability.

For the simulation, rectangular coils measuring one meter by sixty centimeters, with the same values of inductance and size, are considered. The position 0 mm represents the alignment of coil *N* (see Figure 4) and the secondary coil *S* at 100%. At this moment, the coupling coefficient between them is at its maximum. When the secondary coil is positioned halfway between primary coils *N* and $N+1$, in $500\ mm$, the coupling coefficient between coil *N* and coil *S* reaches its minimum used value. To compensate for this variation and maintain the resonance condition at every relative position, the frequency of the primary voltage needs to be regulated.

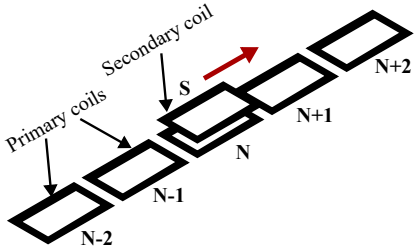


Fig. 4. Primary and secondary coils for the DWPT system.

At the maximum coefficient shown in Figure 3, the frequency applied should be at its maximum value, and at the minimum coupling coefficient, the frequency is at its minimum value. The variation of the frequency will follow the variation of the coupling coefficient. This variation and behavior can be demonstrated considering a system with only two coils, one on the ground and a second inside the vehicle.

Taking the generic equation (1) and applying it to two coils, one on the ground and a second inside the vehicle:

$$v_n = r_n i_n + j\omega L_n i_n + \frac{1}{j\omega C} i_n + j\omega M i_s \tag{6}$$

$$0 = r_s i_s + j\omega L_s i_s + \frac{1}{j\omega C} i_s + j\omega M i_n + R_{ch} i_s \tag{7}$$

where, $v_n$ and $i_n$ are the voltage and current on the primary side, $i_s$ is the current on the secondary side, and M is the mutual inductance between them. $L_n$ and $L_s$ are the inductance on the primary and secondary sides respectively. $R_{ch}$ is an equivalent resistance used to emulate the power load connected on the secondary side.

By isolating the secondary current of (7) and replacing it in (6), the input impedance of the coupled system can be written as:

$$\frac{v_n}{i_n} = r_n + \frac{\omega^2 M^2 \left(r_s + R_{ch}\right)}{\left(r_s + R_{ch}\right)^2 + \left(\omega L_s - \frac{1}{\omega C}\right)^2} + j\left(\omega L_n - \frac{1}{\omega C} - \frac{\omega^2 M^2 \left(\omega L_s - \frac{1}{\omega C}\right)}{\left(r_s + R_{ch}\right)^2 + \left(\omega L_s - \frac{1}{\omega C}\right)^2}\right)$$

Considering the mutual inductance $M = kL$ and taking the imaginary part and solving it to zero, to assure the resonant condition, (8) can be expressed, excluding the two solutions equal to zero for the frequency:

$$\omega^4 \left(L^2 C^2 \left(1 - k^2\right)\right) + \omega^2 \left(C^2 \left(r + R_L\right)^2 - 2LC\right) + 1 = 0 \tag{8}$$

The positive solutions of (8), can be calculated by the following equation:

$$\omega_{1,2} = \sqrt{-\frac{\left(C^2 \left(r + R_L\right)^2 - 2LC\right)}{2L^2 C^2 \left(1 - k^2\right)}} \pm \frac{\sqrt{\left(C^2 \left(r + R_L\right)^2 - 2LC\right)^2 - 4L^2 C^2 \left(1 - k^2\right)}}{2L^2 C^2 \left(1 - k^2\right)} \tag{9}$$

It can be seen that when the value of $k$ increases, the denominator of the equation reduces faster than the numerator. Therefore, a small value of $k$ implies a small value of frequency and a large value of $k$ implies a higher frequency value.

The control algorithm is implemented on the primary side of the DWPT system to tune the resonant frequency by tracking the phase between the output voltage and current of the converter. Figure 5 shows the flow chart of the phase control algorithm. It can be understood as a modified extremum seeking control (see [34], [56] for preliminary versions). The parameter $j$ in the algorithm represents the interaction counter.

The following steps describe the algorithm:

- Step 1 - When the system is initialized, the ground inverter starts with the switching frequency ($f$) used in the previous coil.
- Step 2 - The measurement of the phase angle between the output voltage of the inverter and the output current ($\delta$) is performed. The phase is measured through a zero-crossing circuit for the current and voltage. An electronic circuit transforms the current into a two-level signal to simplify and filter the current zero-crossing. The control sample used is 100 $\mu$s.
- Step 3 - It is verified whether the measured phase for this interaction $\delta(j)$ is between 10° and 15° (to maintain the ZCS condition of the ground converter and ensure the system operates close to the resonant frequency). If

the result is positive, the switching frequency remains unchanged. If negative, the algorithm proceeds to step 4.

- Step 4 - The angle is verified to be higher or lower than 10°. This is performed to determine whether an increase or decrease in the switching frequency is necessary (steps 5 and 6, respectively). The maximum and minimum steps in switching frequency ($\Delta f_{max}$ and $\Delta f_{min}$) are defined to be $110Hz$ and $27.5Hz$, respectively, representing 1% and 0.25% of the available frequency range described in step 7 (from $79kHz$ to $90kHz$, $11kHz$ available range).
- Step 5 - The switching frequency is increased by $\Delta f_{max}$ or $\Delta f_{min}$, depending on the measured angle.
- Step 6 - The switching frequency is decreased by $\Delta f_{max}$ or $\Delta f_{min}$, depending on the measured angle.
- Step 7 - It is checked if the switching frequency is between the limits of $79kHz$ and $90kHz$, following the standard SAE J2954 [54]. If affirmative, the switching frequency is defined as in steps 5 or 6. If negative, the switching frequency is saturated to its limit.
- Step 8 - The switching frequency is defined, and a new verification starts.

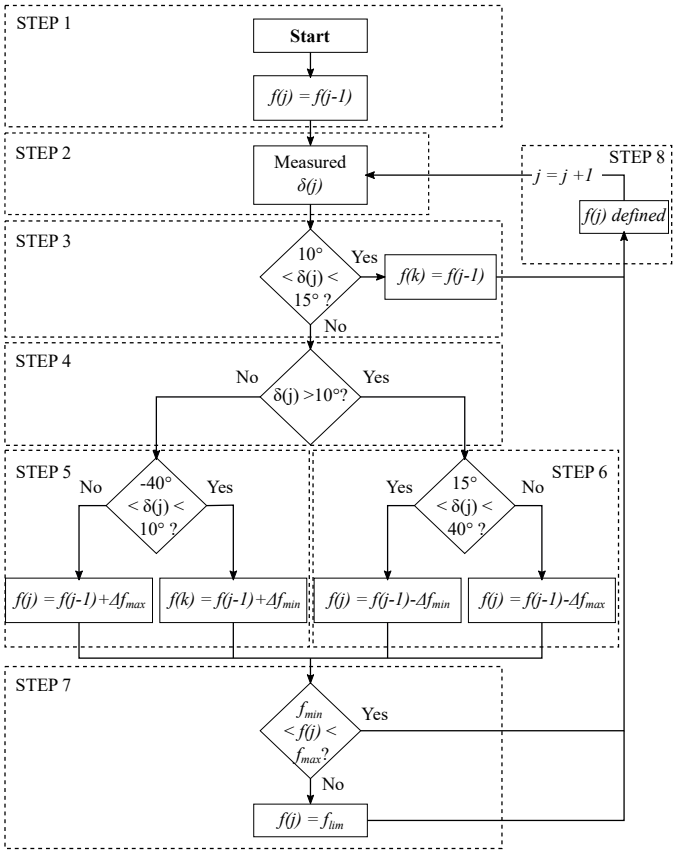


Fig. 5. Flow chart of the phase control algorithm.

## IV. Coil Sequencing

The general architecture of an electrical track is represented in Figure 4. In addition to the Figure, a common DC bus is used to supply the successive coils designated by $N-2$, $N-1$, $N$, $N+1$, and $N+2$ through a sequence of inverters. The secondary coil is also represented in the figure. The direction of movement of the secondary coil is indicated by the red arrow.

The coil sequencing methodology employed in this study uses the existing current sensor within the ground inverters. Consequently, adjacent coils to the active coil are maintained in a short-circuit condition to ensure the continuity of current flow. This configuration is shown in Figure 6 (a), where, with converter $N$ providing power, coils $N+1$ and $N-1$ are rendered in a short-circuit state. During sequencing (the next transmitter coil is activated), as illustrated in Figure 6 (b) (receiver coil 50 cm misaligned), coil $N$ switches to short-circuit mode, while coil $N+1$ switches to active mode, powered by its respective inverter. Simultaneously, coil $N-1$ transitions to the off mode and the coil $N+2$ transitions to the short-circuit mode, thereby replicating the prior system configuration. The color in the coil nomenclature denotes their respective operational states.

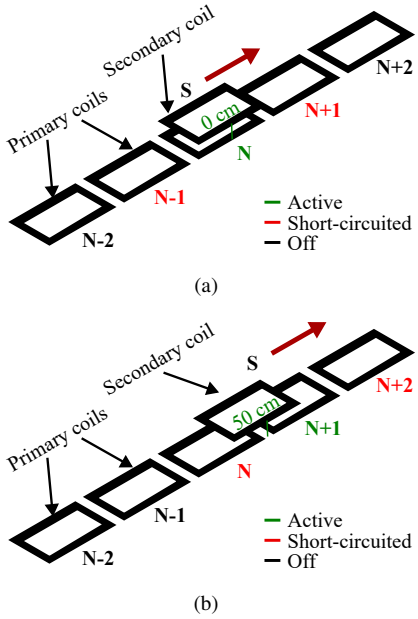


Fig. 6. Coil sequencing. (a) Coil $N$ active. (b) Coil $N+1$ active.

Considering only the effects of the neighboring coils at the switching moment, a small portion of the system with two coils on the ground and one coil inside the vehicle is taken into account. Applying (3) to these three coils:

$$\begin{bmatrix} \lambda_n \\ \lambda_s \\ \lambda_{np1} \end{bmatrix} = \begin{bmatrix} L_n & M_{ns} & M_{nnp1} \\ M_{sn} & L_s & M_{snp1} \\ M_{np1n} & M_{np1s} & L_{np1} \end{bmatrix} \begin{bmatrix} i_n \\ i_s \\ i_{np1} \end{bmatrix} \quad (10)$$

Assessing the symmetric system proposed at the switching time, the secondary coil is at position 500 mm, which means it is located between the two primary coils. The mutual inductance between each primary coil and the secondary coil is the same and is denoted as $a$. The mutual inductance between the primary coils is denoted as $b$, (10) can be written as:

$$\begin{bmatrix} \lambda_n \\ \lambda_s \\ \lambda_{np1} \end{bmatrix} = \begin{bmatrix} L_n & a & b \\ a & L_s & a \\ b & a & L_{np1} \end{bmatrix} \begin{bmatrix} i_n \\ i_s \\ i_{np1} \end{bmatrix}$$

The coils of the presented system are designed to have a minimum coupling coefficient between the primary and secondary coils when the coils are 50% misaligned. Therefore, three different situations are possible:

$a > b$: In this situation, the coupling between the primary coils and the secondary coils is larger than the coupling between the primary coils. This situation favors energy transfer between primary and secondary.

$a < b$: In this situation, the coupling between the primary coils and the secondary coils is smaller than the coupling between the primary coils. This situation needs to be avoided to allow a good energy transfer at the switching time. A small coupling may cause reduced or empty energy transfer at each coil switching.

$a = b$: In this situation, the coupling between primary and secondary coils is similar to the coupling between the primary coils. This is a limited situation to keep a good energy transfer between primary and secondary.

In an ideal system, the coupling coefficient between the primary coils should ideally tend towards zero, while the coupling between the primary and secondary coils must be optimized to maximize the power transfer. Consequently, the $a > b$ condition is preferred and is established as a design requirement for the system. At the transition moment, the current in coil $N$ is nearly equivalent in amplitude to the current in the short-circuited coil $N+1$. The inverters analyze the amplitudes and once the current in coil $N$ closely matches the induced current in coil $N+1$, the sequencing command can be executed to change the states of the coils.

However, in a practical system, the current amplitudes are not identical. They are dependent on different factors such as vehicle height, misalignment, and construction tolerances. To mitigate real-world discrepancies, the transition time is determined based on another current ratio; for example, when the current in coil $N+1$ exceeds 75% of the current in coil $N$. This ratio needs to be selected to satisfy all the necessary requirements of the inductive dynamic charging system, accommodating variations in vehicle heights, misalignment, and interoperability of different coils.

In order to illustrate the relationship between the current at $N$ and $N+1$, equation (1) can be resolved for the three coils (one active and two short circuited, Figure 6) in the system under consideration:

$$v_n = R_n i_n + j\omega L_n i_n + \frac{1}{j\omega C_n} i_n + j\omega M_{ns} i_s + j\omega M_{nnp1} i_{np1} \tag{11}$$

$$0 = R_s i_s + j\omega L_s i_s + \frac{1}{j\omega C_s} i_s + j\omega M_{sn} i_n + j\omega M_{snp1} i_{np1} + R_L i_s \tag{12}$$

$$0 = R_{np1} i_{np1} + j\omega L_{np1} i_{np1} + \frac{1}{j\omega C_{np1}} i_{np1} + j\omega M_{np1s} i_s + j\omega M_{np1n} i_n \tag{13}$$

For analytical simplification, the intrinsic resistances of the coils are disregarded ($R_1 = R_2 = R_3 = 0$), and the frequency is set at resonant frequency $\omega = \frac{1}{\sqrt{LC}}$. This means that $\omega = \frac{1}{\sqrt{LC}} \Rightarrow \omega^2 = \frac{1}{LC} \Rightarrow \omega L = \frac{1}{\omega C}$,

$$v_n = j\omega a i_s + j\omega b i_{np1} \tag{14}$$

$$0 = j\omega a i_n + j\omega a i_{np1} + R_L i_s \tag{15}$$

$$0 = j\omega a i_s + j\omega b i_n \tag{16}$$

therefore,

$$i_{np1} = \left( \frac{R_L b}{j\omega a^2} - 1 \right) i_n \tag{17}$$

demonstrating that $i_n$ exhibits an amplitude comparable to $i_{np1}$ due to the influence of the term $\frac{R_L b}{j\omega a^2} \ll 1$. The current ratio is systematically calibrated during the testing phase to maximize applicability across a wide range of applications.

## V. Modified Extremum Seeking Phase Control and Coil Sequencing Validation Using Simulation

The model is implemented in MATLAB / Simulink Simscape Electrical with the parameters shown in Table II. The simulation is performed considering five coils on the primary side, with mutual inductance adjusted as in Figure 3, to emulate vehicle displacement. Figure 7 illustrates the behavior of the electric track when a DWPT equipped vehicle is on the road and faces road-integrated coils. The results are obtained for a car speed of 60 $km/h$, where the DC bus voltage, the output voltage of the inverter 3, the RMS current of the DC bus and the output current of the inverter 3 are presented. The *DC Bus RMS Current* flows through different converters, while the *Inverter 3 output current* shows the current flowing in coil 3.

TABLE II
DWPT System Simulation Parameters

| Parameter | Value |
|---|---|
| Transferred power | 30 kW |
| DC input voltage | 430 V |
| Coupling coefficient | from 0.1 to 0.26 |
| Primary and secondary inductances | $L_p$ = $L_s$ = $L$ = 135 $\mu$H |
| Primary and secondary resistance | $r_1$ = $r_2$ = $r_s$ = 0.1 $\Omega$ |
| Output Filter Capacitor | $C_f$ = 600 $\mu$F |
| Primary and secondary resonant capacitor | 33 $n$F |
| Inverter switching frequency | 79 to 90 kHz |
| Buck inductor | 100 $\mu$H |
| Battery nominal voltage DS3 | 350 to 450 V |
| Battery current reference | 65 A |

For this simulation, the system starts with coil 1 well aligned with the secondary coil, and its inverter works at a fixed switching frequency of 81 kHz to avoid over-current and over-voltages. With the car moving, the coupling of the secondary coil 2 increases, increasing the induced current. When the induced current in coil 2 reaches approximately 50% (this is used just for the first coil, because of the fixed frequency, for all others the value of 75% is used) of the current in coil 1, the second inverter is turned on and the first inverter is turned off, changing the coil 1 for short-circuit mode. At this moment,

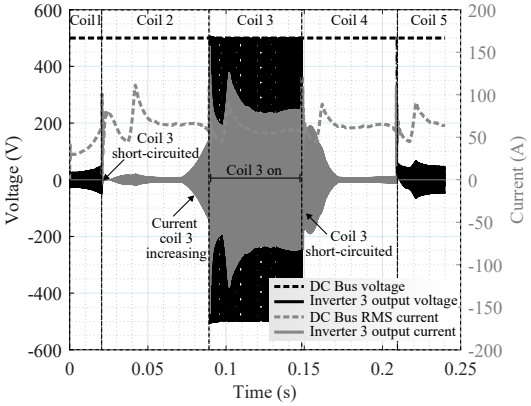


Fig. 7. Electric track behavior for the DWPT system under study.

coil 3 is also short-circuited. This is represented in Figure 7 by the voltage and current in the third inverter, when coil 2 is turned on and the coil 3 is short-circuited, the inverter 3 output voltage is zero and the current starts to increase, according to the position of the car.

At the moment that the induced current in coil 3 is $75\%$ of current in coil 2, coil 3 is turned on, coil 2 is short-circuited to turn the inverter off, and coil 4 is short-circuited for car detection. The transition between coils 2 and 3 is shown in Figures 8 (a) and (b). Where Figure 8 (a) emphasizes the current increasing in coil 3, and the moment that this coil is turned on, and Figure 8 (b) emphasizes the current in coil 2 decreasing when it is short-circuited.

As discussed in Section III the control algorithm adjusts the switching frequency to ensure the ZCS when the converter works close to the resonance frequency. In Figure 9 the voltage and current waveforms for inverter 3 output are shown. In this, the phase between voltage and current is controlled to be between $10°$ and $15°$ (as explained in the flow chart of the control algorithm in Figure 5), ensuring the inverter ZCS operation.

The waveforms for the secondary side are presented in Figure 10. A battery voltage of 400 V is used and a constant current of $65\ A$ is requested by the buck converter.

## VI. Experimental Results

The experiments are carried out in full-scale tests considering the same parameters of Table II. In Figure 11 the test setup is shown. In this, 18 coils are integrated into a ground trench, represented by number 3 in the figure. Inside the vehicle is embedded a coil with parameters identical to those of the primary coils (number 4). The vehicle is a *Stellantis DS3 Crossback* (number 1). Within the car, a rectifier and a DC/DC buck converter are installed and configured to request 30 kW (number 6). The DC/DC output is connected to the vehicle battery via a circuit-breaker box for security. Inverters are positioned alongside the road (number 2) and supplied with a 430 VDC power source (number 5). Similarly to the previous model, each primary coil is equipped with an inverter. The DC bus voltage and power are provided by ITECH IT6000D with 7 modules connected in parallel.

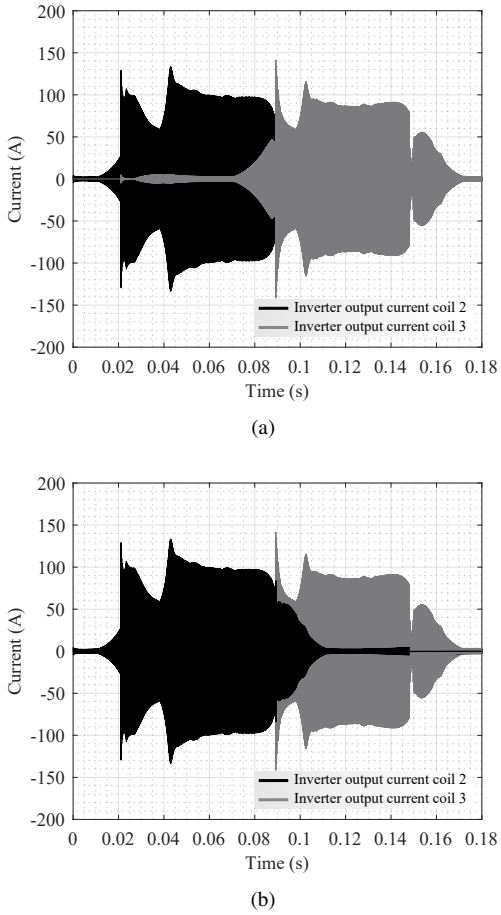


Fig. 8. Transition between coils two and three. (a) Emphasize the current increase in coil three. (b) Emphasize the current in coil two decreasing.

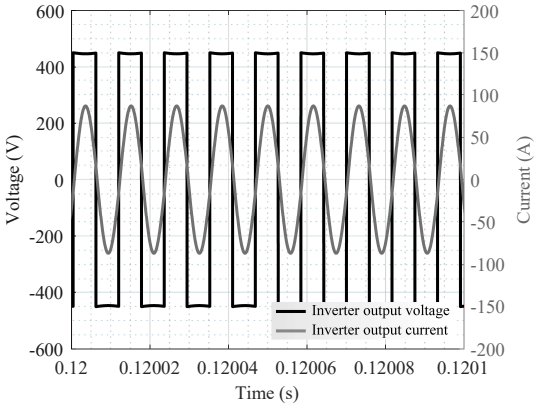


Fig. 9. Voltage and current waveforms for inverter three output.

As described in Section IV, only one primary coil is powered at any given time. The first primary coil is activated with a fixed frequency of $81\ kHz$ to synchronize the system and prevent security protections from triggering. The second primary coil is activated when its current reaches approximately 50% of the current in the first coil. It is important to note that the neighboring coils of the active one are constantly in a short-circuit state, with induced current continuously

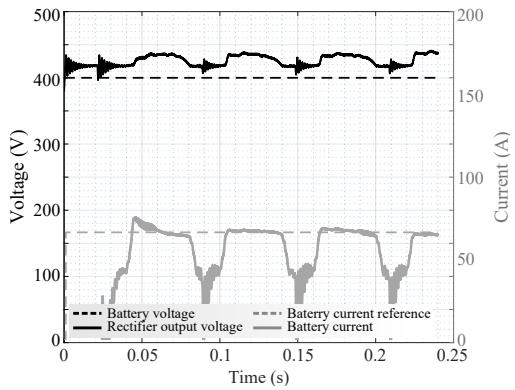


Fig. 10. Voltage and current waveforms for the secondary side.

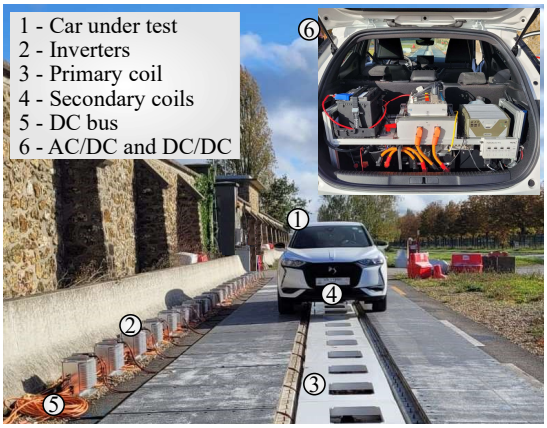


Fig. 11. Experimental setup using an electric road.

flowing. For the switching process of the subsequent primary coils, the sending power is already established, and it follows as described in previous sections of this work.

In Figure 12 the currents of primary coil 2 (in pink) and coil 3 (in green) at the moment of the transition states are depicted. In Figure 12 (a), the induced current coil 3 (in green) starts to increase before the transition moment. At the switching time, the current in coil 2 stops growing and suddenly drops to a value close to that of coil 3. Subsequently, it transitions to inductive behavior before dropping to near zero as the secondary coil moves away. Figure 12 (b) is the same as Figure 12 (a) but with the current in coil 2 highlighted. In Figure 12 (c), a zoomed-in view of the exact moment of the transition can be observed.

During the entire process, the ZCS condition is maintained by the control strategy introduced in previous sections. In Figure 13, the system operating in ZCS is shown for 5 cycles. At the instant of measurement, the switching frequency is $88.5\ kHz$, and the phase between current (green) and voltage (blue) is 16°.

The dynamic charging is illustrated in Figure 14. In the ground-side waveforms (Figure 14 (a)), the DC voltage and current at the inverter input are represented by lines C1 (yellow) and C2 (pink) respectively. Lines C3 (blue) and C4 (green) represent the voltage and current in the fourth coil.

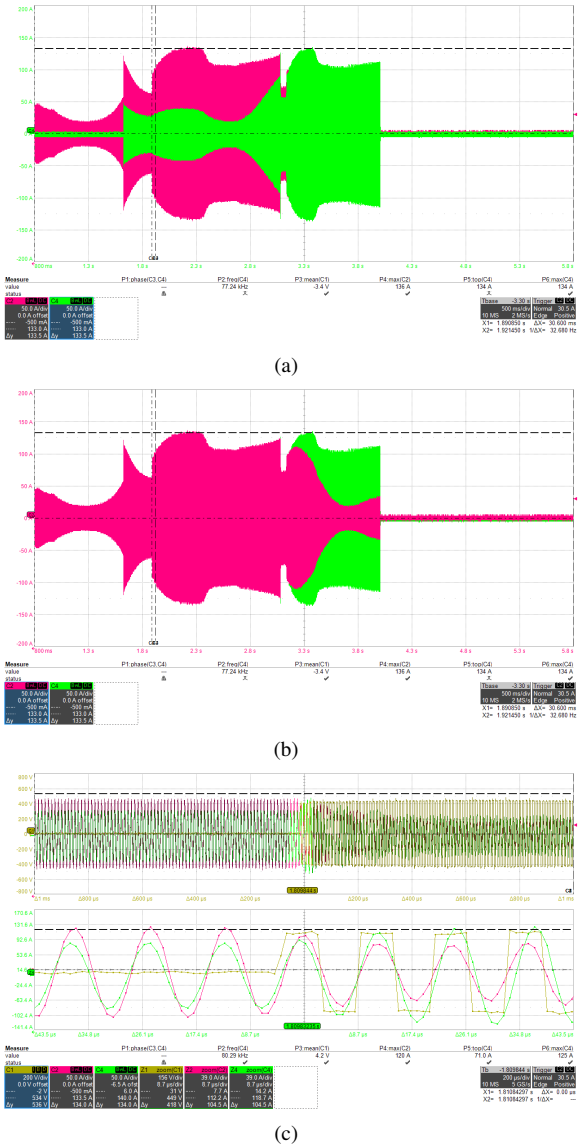

(a)

(b)

(c)

Fig. 12. Transition between coil 2 and 3. (a) Current in coil 3 (green) highlighted. (b) Current in coil 2 (pink) highlighted. (c) Zoom for the transition moment.

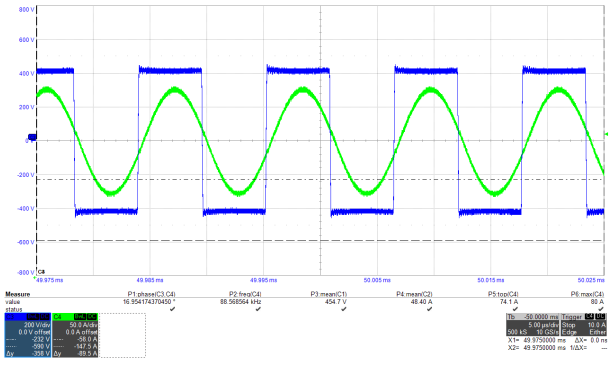

Fig. 13. System working at ZCS.

Figure 14 (b) shows the DC bus voltage in the rectifier output (yellow) and the current supplied to the battery (pink) . Here, the battery current reference is set to 65 A.

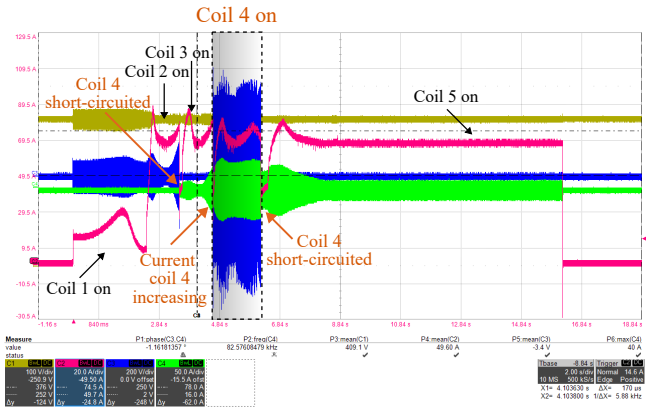


(a)

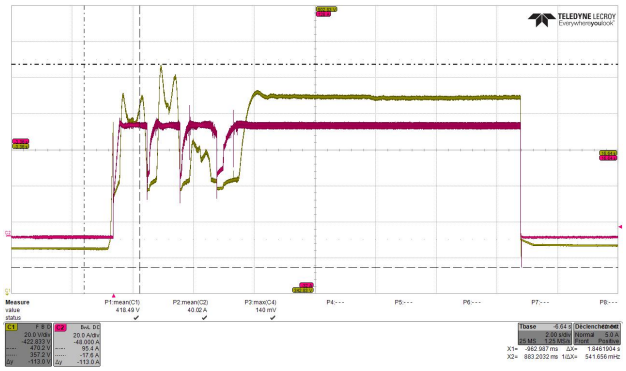

(b)

Fig. 14. Dynamic charging. (a) Ground side waveforms. (b) Secondary side waveforms.

In Figure 14 (a), coil 4 behavior is described. The information shown in orange pinpoints the time instants when this coil is first placed in a short-circuit state; then when the current increases; the time while this coil is activated (starting when the induced current reaches 75% of the value of the current in coil 3); and the moment when it is placed back in a short-circuit state (when coil 5 is turned-on). The moments when other coils are activated are identified by the name of the coil marked in black. In this figure, the input power is 29.88 $kW$ and the output power is 27.08 $kW$, resulting in an efficiency of 90.6% (from DC bus to battery including the inverter, the coils and the induction process, the rectifier, and the DC/DC converter).

The DC bus voltage in the rectifier output (yellow) and the current supplied for the battery (pink) in the case of 18 coils on the primary side are shown in Figure 15. Here, the battery current reference is set to 65 A, and measurements are performed with the vehicle at 15.7 $km/h$. Similar systems have already been tested at speeds close to 70 $km/h$.

By analyzing the results, it is shown that the switching procedure and ZCS conditions are satisfied as predicted in the model and simulations, as well as the transition among the coils and the system's capacity to provide the power required by the secondary side. It is worth mentioning that for experimental results, alignment, and velocity are not guaranteed because they depend on the driver.

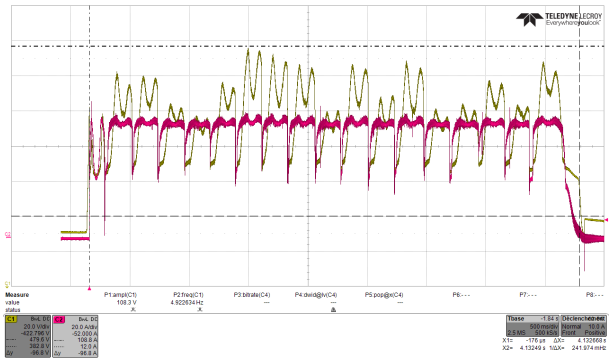

Fig. 15. Dynamic charging secondary side waveforms for 18 coils on the primary side.

## VII. Discussions

The presented DWPT system successfully demonstrated continuous energy transfer for electric vehicles traveling on an 18 meter electrical road. Full-scale experiments are performed using a DS3 Crossback vehicle to recharge up to 30 kW. They achieved an efficiency of 90.6% from the DC bus to the battery, including the inverter, the coils and the induction process, the rectifier, and the DC/DC converter. This validated the theoretical models. These results are obtained by employing primary coils embedded along the road, in combination with the sequencing technique for coil activation, and the use of the modified extremum seeking control, which showed significant improvements in maintaining power delivery and system stability during dynamic charging conditions.

The sequencing technique used ensures efficient coil activation without requiring the use of additional sensor hardware, simplifying the system architecture while maintaining robust power transfer. The modified extremum seeking control effective tracks the resonance frequency, thereby ensuring soft-switching and maintaining zero-current switching (ZCS) during power transfer. These results highlight the ability of the system to maintain high performance when the vehicle is in motion.

The performance of the DWPT system is consistent with the findings of previous research on dynamic charging systems, such as those presented by [38] and [39]. However, the presented approach to coil selection and activation without relying on position sensors represents an advancement over previous designs that often depend on additional hardware for vehicle detection and coil alignment. By focusing on a current-based selection mechanism, this work simplifies the control strategy while ensuring accurate coil activation.

The ability to recharge a vehicle dynamically, while maintaining power transfer efficiency, could extend the autonomy of electric vehicles and reduce the need on large onboard batteries. This reduces not only the weight and cost of electric vehicles, but also the frequency of stops to recharging, making long-distance EV travel more feasible. This could also lead to a significant reduction in greenhouse gas emissions and further promote the use of renewable energy sources in transportation.

## VIII. Conclusion

This paper presented a Dynamic Wireless Power Transfer (DWPT) system designed for electric roads, with a primary focus on powering electric vehicles during long-haul freight transportation. The system incorporates primary coils along the road, DC/AC converters, and a power receiver coil within the vehicle. The paper introduces the DWPT system, outlines a coil selection strategy, presents a system model, and discusses a phase angle control mechanism, based on extremum seeking, to optimize power transfer.

Experimental tests conducted on a Stellantis DS3 Crossback vehicle validate the system's ability to maintain power and voltage stability under varying coupling coefficients. The experiments used 18 primary coils within a ground trench. The DS3 Crossback vehicle is equipped with a matching coil, a rectifier, and a DC/DC buck converter, with safety systems such as a circuit-breaker box connecting the DC/DC output to the vehicle battery. Inverters are placed alongside the road and supplied with a 430 VDC power source, with only one primary coil activated at any given time. The control strategy maintained zero-current switching (ZCS) during the switching process, ensuring a smooth transition between coils. The results of these experiments confirm that the system operates as predicted in the models and simulations. In the experiments, the input power in the DC bus was $29.88\ kW$, while the output power (in the battery) was $27.08kW$ with an efficiency of 90.6% from DC bus to battery.

While the results are promising, there are limitations to the current system that must be addressed in future work. One of the primary challenges is ensuring consistent energy transfer under varying road conditions, such as irregular surfaces or inclement weather, which were not fully tested in the presented experiments. Furthermore, the efficiency of 90.6% observed in the experiments can be improved by designing the system using optimization techniques. In addition, the cost-effectiveness of large-scale DWPT deployment remains to be studied, especially in terms of infrastructure requirements and maintenance costs.

Finally, scaling the system for use in high-traffic environments will require investigation of more advanced power management strategies, possibly integrating vehicle-to-grid (V2G) technology to optimize energy distribution across multiple vehicles. Long-term reliability testing under real-world conditions will also be essential to ensure the commercial viability of DWPT systems for both passenger and freight vehicles.

## Acknowledgment

This work has received funding from the European Union's Horizon 2020 research and innovation program under Grant Agreement No 875683 (Incit EV project) and from the CNPq (175271/2023-2) and CAPES/PROEX - Finance Code 001.

## Appendix

### A. Notation list

- $a$: mutual inductance between each primary coil and the secondary coil;
- AC: Alternate Current;
- $b$: mutual inductance between the primary coils;
- $\hat{C}$: matrix of capacitors.
- $C$: resonant tank capacitor;
- $C_f$: output filter capacitor
- DC: Direct Current;
- DWPT: Dynamic Wireless Power Transfer;
- EVs: Electric Vehicles;
- $f$: switching frequency;
- $\hat{I}$: vector of the currents flowing in the coils;
- $i_n$: current in the primary coil;
- $i_s$: current in the secondary coil;
- $j$ : interaction counter for the algorithm;
- $k$: coupling coefficient;
- $L$: self-inductance
- $L_n$: self-inductance of the coil $n$;
- $L_p$: primary self-inductance
- $L_s$: secondary self-inductance
- M: mutual inductance between primary and secondary coils;
- $M_{n.np1}$: mutual inductance between the coil $n$ and its neighbor coil $np1$;
- $M_{n.s}$: mutual inductance between the coil $n$ and the secondary coil $s$;
- $n$: subscript that refers to the primary coil;
- $nm1$: primary coil in position $N-1$;
- $np1$: primary coil in position $N+1$;
- $np2$: primary coil in position $N+2$.
- $\hat{R}$: matrix of the resistances;
- $R_{ch}$: equivalent resistance used to emulate the power load connected on the secondary side.
- $r_n$: self-resistance of the coil wire;
- $s$: subscript that refers to the secondary coil;
- SoH: State of Health;
- $v$: speed of the secondary coil;
- $\hat{V}$: vector of the voltages applied or induced in the coils;
- $\hat{V}_C$: vector of the voltages across the resonant capacitors;
- $v_{C_n}$: voltage across the series resonant capacitor;
- $V_{DC}$: DC voltage;
- $\hat{V}_L$: voltage across the inductors of the coils;
- $v_{L_P}$: voltage across the inductor;
- $v_n$: applied voltage in the primary coil;
- $V_O$: output DC voltage
- $v_s$: secondary AC voltage;
- ZCS: Zero Current Switching;
- ZVS: Zero Voltage Switching;
- $\delta$: phase angle between the inverter output voltage and the output current;
- $\lambda_n$: total flux passing through the coil $n$;
- $\hat{\Lambda}$: matrix for total flux;
- $\omega_r$: fundamental frequency of the resonant network.

## References

[1] G. Bin, L. Chien-Yu, C. Baifeng, J. Dominic, and L. Jih-Sheng, "Zero-voltage-switching pwm resonant full-bridge converter with manimized circulting losses and minimal voltage stresses of bridge rectifiers for electric vehicle battery chargers," *IEEE Transactions on Power Electronics*, vol. 28, pp. 1132–1144, 2013.

[2] H. N. de Melo, J. P. F. Trovao, P. G. Pereirinha, H. M. Jorge, and C. H. Antunes, "A controllable bidirectional battery charger for electric vehicles with vehicle-to-grid capability," *IEEE Transactions on Vehicular Technology*, vol. 67, pp. 114–123, 2018.

[3] J. Deng, S. Li, S. Hu, C. C. Mi, and R. Ma, "Design methology of llc resonant converters for electric vehicle battery chargers," *IEEE Transactions on Vehicular Technology*, vol. 63, pp. 1581–1592, 2014.

[4] X. Mou, O. Groling, and H. Sun, "Energy-efficient and adaptive design for wireless power transfer in electric vehicles," *IEEE Transactions on Industrial Electronics*, vol. 64, no. 9, pp. 7250–7260, 2017.

[5] A. Sagar, A. Kashyap, M. A. Nasab, S. Padmanaban, M. Bertoluzzo, A. Kumar, and F. Blaabjerg, "A comprehensive review of the recent development of wireless power transfer technologies for electric vehicle charging systems," *IEEE Access*, 2023.

[6] A. Kurs, A. Karalis, R. Moffatt, J. D. Joannopoulos, P. Fisher, and M. Soljacic, "Wireless power transfer via strongly coupled magnetic resonances," *science*, vol. 317, no. 5834, pp. 83–86, 2007.

[7] A. König, L. Nicoletti, D. Schröder, S. Wolff, A. Waclaw, and M. Lienkamp, "An overview of parameter and cost for battery electric vehicles," *World Electric Vehicle Journal*, vol. 12, no. 1, p. 21, 2021.

[8] J. Neubauer, A. Pesaran, C. Bae, R. Elder, and B. Cunningham, "Updating united states advanced battery consortium and department of energy battery technology targets for battery electric vehicles," *Journal of Power Sources*, vol. 271, pp. 614–621, 2014.

[9] Á. Cunha, F. Brito, J. Martins, N. Rodrigues, V. Monteiro, J. L. Afonso, and P. Ferreira, "Assessment of the use of vanadium redox flow batteries for energy storage and fast charging of electric vehicles in gas stations," *Energy*, vol. 115, pp. 1478–1494, 2016.

[10] N. B. Arias, S. Hashemi, P. B. Andersen, C. Træholt, and R. Romero, "Distribution system services provided by electric vehicles: Recent status, challenges, and future prospects," *IEEE Transactions on Intelligent Transportation Systems*, vol. 20, no. 12, pp. 4277–4296, 2019.

[11] O. Sadeghian, A. Oshnoei, B. Mohammadi-Ivatloo, V. Vahidinasab, and A. Anvari-Moghaddam, "A comprehensive review on electric vehicles smart charging: Solutions, strategies, technologies, and challenges," *Journal of Energy Storage*, vol. 54, p. 105241, 2022.

[12] B. Nykvist, F. Sprei, and M. Nilsson, "Assessing the progress toward lower priced long range battery electric vehicles," *Energy policy*, vol. 124, pp. 144–155, 2019.

[13] V.-B. Vu, A. Ramezani, A. Triviño, J. M. González-González, N. B. Kadandani, M. Dahidah, V. Pickert, M. Narimani, and J. Aguado, "Operation of inductive charging systems under misalignment conditions: A review for electric vehicles," *IEEE Transactions on Transportation Electrification*, vol. 9, no. 1, pp. 1857–1887, 2022.

[14] J. A. Sanguesa, V. Torres-Sanz, P. Garrido, F. J. Martinez, and J. M. Marquez-Barja, "A review on electric vehicles: Technologies and challenges," *Smart Cities*, vol. 4, no. 1, pp. 372–404, 2021.

[15] K. Kadem, M. Bensetti, Y. Le Bihan, E. Labouré, and M. Debbou, "Optimal coupler topology for dynamic wireless power transfer for electric vehicle," *Energies*, vol. 14, no. 13, p. 3983, 2021.

[16] E. Coca, *Wireless power transfer: fundamentals and technologies*. BoD–Books on Demand, 2016.

[17] M. Yilmaz and P. T. Krein, "Review of battery charger topologies, charging power levels, and infrastructure for plug-in electric and hybrid vehicles," *IEEE transactions on Power Electronics*, vol. 28, no. 5, pp. 2151–2169, 2012.

[18] Z. Moghaddam, I. Ahmad, D. Habibi, and Q. V. Phung, "Smart charging strategy for electric vehicle charging stations," *IEEE Transactions on transportation electrification*, vol. 4, no. 1, pp. 76–88, 2017.

[19] A. Meintz, J. Zhang, R. Vijayagopal, C. Kreutzer, S. Ahmed, I. Bloom, A. Burnham, R. B. Carlson, F. Dias, E. J. Dufek *et al.*, "Enabling fast charging–vehicle considerations," *Journal of Power Sources*, vol. 367, pp. 216–227, 2017.

[20] S. Srdic and S. Lukic, "Toward extreme fast charging: Challenges and opportunities in directly connecting to medium-voltage line," *IEEE Electrification Magazine*, vol. 7, no. 1, pp. 22–31, 2019.

[21] K. Y. Lee, F. Bühs, D. Göhlich, and S. Park, "Towards reliable design and operation of electric road systems for heavy-duty vehicles under realistic traffic scenarios," *IEEE Transactions on Intelligent Transportation Systems*, pp. 1–14, 2023.

[22] H. Zhang, F. Lu, and C. Mi, "An electric roadway system leveraging dynamic capacitive wireless charging: Furthering the continuous charging of electric vehicles," *IEEE Electrification Magazine*, vol. 8, no. 2, pp. 52–60, 2020.

[23] J. Boys, G. Covic, and A. W. Green, "Stability and control of inductively coupled power transfer systems," *IEE Proceedings-Electric Power Applications*, vol. 147, no. 1, pp. 37–43, 2000.

[24] G. A. Covic, J. T. Boys, M. Budhia, and C.-Y. Huang, "Electric vehicles–personal transportation for the future," *World Electric Vehicle Journal*, vol. 4, no. 4, pp. 693–704, 2010.

[25] M. Budhia, G. Covic, and J. Boys, "A new ipt magnetic coupler for electric vehicle charging systems," in *IECON 2010-36th Annual Conference on IEEE Industrial Electronics Society*. IEEE, 2010, pp. 2487–2492.

[26] G. A. Covic, M. Budhia, C.-Y. Huang *et al.*, "Development of a single-sided flux magnetic coupler for electric vehicle ipt charging systems [j]," *IEEE Transactions on Industrial Electronics*, vol. 60, no. 1, pp. 318–328, 2013.

[27] M. Budhia, G. A. Covic, and J. T. Boys, "Design and optimization of circular magnetic structures for lumped inductive power transfer systems," *IEEE Transactions on Power Electronics*, vol. 26, no. 11, pp. 3096–3108, 2011.

[28] Z. Bi, T. Kan, C. C. Mi, Y. Zhang, Z. Zhao, and G. A. Keoleian, "A review of wireless power transfer for electric vehicles: Prospects to enhance sustainable mobility," *Applied energy*, vol. 179, pp. 413–425, 2016.

[29] P. Venugopal, A. Shekhar, E. Visser, N. Scheele, G. R. C. Mouli, P. Bauer, and S. Silvester, "Roadway to self-healing highways with integrated wireless electric vehicle charging and sustainable energy harvesting technologies," *Applied energy*, vol. 212, pp. 1226–1239, 2018.

[30] D. H. Tran, V. B. Vu, and W. Choi, "Design of a high-efficiency wireless power transfer system with intermediate coils for the on-board chargers of electric vehicles," *IEEE Transactions on Power Electronics*, vol. 33, pp. 175–187, 2018.

[31] H. Wang, U. Pratik, A. Jovicic, N. Hasan, and Z. Pantic, "Dynamic wireless charging of medium power and speed electric vehicles," *IEEE Transactions on Vehicular Technology*, vol. 70, pp. 12 552–12 566, 2021.

[32] J.-Y. Lee and B.-M. Han, "A bidirectional wireless power transfer ev charger using self-resonant pwm," *IEEE Transactions on Power Electronics*, vol. 30, pp. 1784–1787, 2015.

[33] K. Kadem, Z. Meira, G. Damm, and H. Moussa, "Efficient sequencing method of ground coils for dynamic wireless power transfer," in *IEEE Wireless Power Week (WPW 2022)*. IEEE, 2022.

[34] Z. Meira, G. Damm, K. Kadem, and H. Moussa, "A 30 kw dynamic wireless inductive charging system for evs," in *24th European Conference on Power Electronics and Applications (EPE'22)*. EPE, 2022.

[35] S. D. Barman, A. W. Reza, N. Kumar, M. E. Karim, and A. B. Munir, "Wireless powering by magnetic resonant coupling: Recent trends in wireless power transfer system and its applications," *Renewable and Sustainable energy reviews*, vol. 51, pp. 1525–1552, 2015.

[36] S. Li, Z. Liu, H. Zhao, L. Zhu, C. Shuai, and Z. Chen, "Wireless power transfer by electric field resonance and its application in dynamic charging," *IEEE Transactions on Industrial Electronics*, vol. 63, no. 10, pp. 6602–6612, 2016.

[37] C. Jiang, K. Chau, C. Liu, and C. H. Lee, "An overview of resonant circuits for wireless power transfer," *Energies*, vol. 10, no. 7, p. 894, 2017.

[38] G. R. Nagendra, L. Chen, G. A. Covic, and J. T. Boys, "Detection of evs on ipt highways," *IEEE journal of emerging and selected topics in power electronics*, vol. 2, no. 3, pp. 584–597, 2014.

[39] Y. Bu, M. Nishiyama, T. Ueda, Y. Tashima, and T. Mizuno, "Examination of wireless power transfer combined with the utilization of distance detection," *IEEE Transactions on Magnetics*, vol. 50, no. 11, pp. 1–4, 2014.

[40] A. Kamineni, M. J. Neath, A. Zaheer, G. A. Covic, and J. T. Boys, "Interoperable ev detection for dynamic wireless charging with existing hardware and free resonance," *IEEE transactions on transportation electrification*, vol. 3, no. 2, pp. 370–379, 2016.

[41] K. Hwang, J. Cho, D. Kim, J. Park, J. H. Kwon, S. I. Kwak, H. H. Park, and S. Ahn, "An autonomous coil alignment system for the dynamic wireless charging of electric vehicles to minimize lateral misalignment," *Energies*, vol. 10, no. 3, p. 315, 2017.

[42] D. Patil, J. M. Miller, B. Fahimi, P. T. Balsara, and V. Galigekere, "A coil detection system for dynamic wireless charging of electric vehicle," *IEEE Transactions on Transportation Electrification*, vol. 5, no. 4, pp. 988–1003, 2019.

[43] C. Cai, M. Saeedifard, J. Wang, P. Zhang, J. Zhao, and Y. Hong, "A cost-effective segmented dynamic wireless charging system with stable efficiency and output power," *IEEE Transactions on Power Electronics*, vol. 37, no. 7, pp. 8682–8700, 2022.

[44] K. Kadem, F. Cheriet, E. Laboure, M. Bensetti, Y. Le Bihan, and M. Debbou, "Sensorless vehicle detection for dynamic wireless power

transfer," in *2019 21st European Conference on Power Electronics and Applications (EPE'19 ECCE Europe)*. IEEE, 2019, pp. P–1.
[45] L. Serge and C. Antoine, "Procedé de charge sans contact dynamique, et système correspondant," 6 2017, Renault SAS. [Online]. Available: https://worldwide.espacenet.com/patent/search/family/055646725/publication/FR3045231A1?q=pn%3DFR3045231A1
[46] W. Kabbara, M. Bensetti, T. Phulpin, A. Caillierez, S. Loudot, and D. Sadarnac, "A control strategy to avoid drop and inrush currents during transient phases in a multi-transmitters dipt system," *Energies*, vol. 15, no. 8, p. 2911, 2022.
[47] S. Li, L. Wang, Y. Guo, and Z. Liu, "Flexible energy-transfer control of dynamic wireless power transfer system based on estimation of load and mutual inductance," *IEEE Transactions on Industry Applications*, vol. 58, no. 1, pp. 1157–1167, 2021.
[48] A. Alkasir, S. E. Abdollahi, S. R. Abdollahi, and P. Wheeler, "Enhancement of dynamic wireless power transfer system by model predictive control," *IET Power Electronics*, vol. 15, no. 1, pp. 67–79, 2022.
[49] N. Mohamed, F. Aymen, T. E. A. Alharbi, C. Z. El-Bayeh, S. Lassaad, S. S. M. Ghoneim, and U. Eicker, "A comprehensive analysis of wireless charging systems for electric vehicles," *IEEE Access*, vol. 10, pp. 43 865–43 881, 2022.
[50] J. Liu, X. Zhang, J. Yu, Z. Xu, and Z. Ju, "Performance analysis for the magnetically coupled resonant wireless energy transmission system," *Complexity*, vol. 2019, no. 1, Jan. 2019.
[51] E. O. Prado, P. C. Bolsi, H. C. Sartori, and J. R. Pinheiro, "An overview about si, superjunction, sic and gan power mosfet technologies in power electronics applications," *Energies*, vol. 15, no. 14, p. 5244, 2022.
[52] A. Caillierez, "Etude et mise en oeuvre du transfert de l'énergie électrique par induction: application à la route électrique pour véhicules en mouvement," Ph.D. dissertation, Université Paris Saclay (COmUE), 2016.
[53] P.-A. Gori, "Transmission dynamique d'énergie par induction : application au véhicule électrique," Theses, Université Paris Saclay (COmUE), Oct. 2019. [Online]. Available: https://theses.hal.science/tel-02413595
[54] SAE International. (2022, August) Wireless power transfer for light-duty plug-in/electric vehicles and alignment methodology. http://standards.sae.org/j2954_202208/.
[55] A. C. Bagchi, A. Kamineni, R. A. Zane, and R. Carlson, "Review and comparative analysis of topologies and control methods in dynamic wireless charging of electric vehicles," *IEEE Journal of Emerging and Selected Topics in Power Electronics*, vol. 9, no. 4, pp. 4947–4962, 2021.
[56] H. Moussa, Z. M. Gomes, K. Kadem, and G. Damm, "Modeling and control of dynamic wireless power transfer system for electric vehicle charger application," in *IFAC World Congress 2023*. Yokohama, Japan: IFAC, July 9-14 2023.

**Zariff Meira Gomes,** holds a Master's degree (2015) in Electrical Engineering from the Federal University of Paraíba (UFPB). Currently pursuing a Ph.D. in Electrical Engineering at the Federal University of Bahia (UFBA). From 2017 to 2023, worked at VEDECOM Institut as the Project Leader for Automated Charging Systems. From 2023 to 2024, served as the Smart Charging and V2G Product Specialist at Nissan. Since then, has been working as an EV Charging Systems Expert at IVECO Group. Main areas of interest include design, modeling, simulation, prototyping, real-time programming, electrical machines, EV charging systems, V2G, smart charging, wireless power transfer, energy conversion, and power electronics applications.

**Edemar de Oliveira Prado** holds master's (2020) and Ph.D. (2024) degrees in Electrical Engineering from the Federal University of Santa Maria (UFSM). Currently, he is pursuing a Ph.D. in Electrical Engineering at the Federal University of Bahia (UFBA) and is enrolled in a postdoctoral program at UFSM. From 2023 to 2024, he completed a sandwich Ph.D. in France, collaborating with the Gustave Eiffel University and the VEDECOM Institute. He has experience in the area of Electrical Engineering, working mainly on the following topics: Renewable energy sources integrated into UPSs and ESSs; Evaluation of modulation techniques, thermal design, and converter optimization; Design, modeling, and control of dynamic wireless power transfer systems for electric vehicles.

**Yann Le Gall** Holds a master's degree (2021) in electronics and electrical energy from Rennes 1 University in France. He has been working at the VEDECOM Institute since 2022 as an embedded systems developer. His main areas of activity are real-time system programming, prototyping and wireless energy transfer.

**Gilney Damm** is a Senior Research Scientist (Directeur de Recherche) at University Gustave Eiffel, at the Laboratoire COSYS-IMSE. Previously, he was an Associate Professor at the Paris-Saclay University, CentraleSupelec, France. He is an Electronic Engineer – Automatic Control from the Rio de Janeiro Federal University – Brazil, and PhD from CentraleSupelec - Paris-Saclay University. His research interests concern nonlinear and adaptive control and observers applied to power systems (SmartGrids, SuperGrid, MicroGrids). His main applications are in the field of large-scale integration of renewable energy and electric vehicles; Multi-Terminal HVDC systems; Mixed AC/DC MicroGrids; Control of Power Systems and Power Electronics in high and low voltage, AC and DC (transient stabilization, frequency, and voltage stability, synthetic inertia, grid forming converters); synchronization of power networks; energy integration in SmartCities; Dynamic recharging of electric vehicles (along the road). He has a large experience as a coordinator or Work-Package Leader in several European and French research projects, in particular the Institutes for Energy Transition SuperGrid (on large-scale high voltage electrical grids), Efficacity (on MicroGrids and SmartCities) and Vedecom (on dynamic inductive charging of electric vehicles). He is a member of the IFAC Technical Committee TC 6.3 Power and Energy Systems since 2015. He has been Associate Editor at the European Journal of Control since 2010 and Energies since 2020.

**Christophe Ripoll** worked at Renault Group from 1994 to the present, holding multiple roles in research and development, safety, and leadership. Currently, he is the lead of the research team, focusing on innovative charging systems, including a 30 kW inductive charger and a conductive charging demonstrator. Previously managed homologation and safety for electric vehicles, developing safety specifications for Renault-Nissan. He has experience in power electronics, contributing to the development of 22 kW and 43 kW chargers, designing safety systems for EV chargers. Early roles included developing embedded software for HVAC systems and prototyping robotic gearboxes and piezoelectric injector controls. Before joining Renault, he worked as an engineering consultant at Altran, designing resonant converters and high-voltage generators for industrial applications.

**José Renes Pinheiro** holds a degree in Electrical Engineering from the Federal University of Santa Maria/UFSM (1981), master's degree in electrical engineering from the Federal University of Santa Catarina (1984), PhD in Electrical Engineering from the Federal University of Santa Catarina (1994), and post-doctorate from Virginia Tech, VA, USA (2002). From 2018 to 2024, he got a position as Visiting Professor at the PPGEE of the Federal University of Bahia. He is currently a Titular Professor at the University of Itajaí Valley (UNIVALI), a Volunteer Professor at the Departments of Electrical and Computer Engineering (UFBA) and Electrical Energy Processing (UFSM), and Permanent Professor of the Graduate Programs in Electrical Engineering at the Federal University of Santa Maria and the Federal University of Bahia. In 1987, he was one of the founders and leader of the Power Electronics and Control Group (GEPOC) to this day. Between 2006 and 2015, he was the coordinator of the PPGEE (CAPES – Level 7) at UFSM. He was the Technical Program Coordinator of the Brazilian Congress on Power Electronics (COBEP) in 1999, and the mentor of the IEEE Seminar on Power Electronics and Control (IEEE SEPOC) in 2000 and coordinated it in 2005 and 2017. He is the author and co-author of more than 450 technical papers published in scientific conferences and journals. Dr. Pinheiro is a member of the Brazilian Society of Power Electronics, the Brazilian Society of Automatics, and the IEEE Societies PELS, IAS, IES and PES. In 2015 he was a founder of the IEEE Joint Chapter, and in 2016 of the UFSM/IEEE Student Branch. He was also one of the founders and first director of the Smart Grids Institute INRI, which currently hosts the INMETRO-accredited laboratories: Photovoltaic Testing Laboratory and the Medium and High Voltage Laboratory, as well as the INCT in Distributed Electric Energy Generation, where he serves as vice coordinator. He has a very relevant track record of 5 book chapters, +100 scientific articles in journals, and +400 in conferences. As well as, in Google Scholar, in January 2025, he had 6804 citations and h-index 41. His main lines of research and interest include Optimized Designs of Static Converters, Hybrid Multilevel Converters, Hybrid Static Energy Conversion Systems, High Frequency Energy Conversion, Modeling and Control of Static Converters, Transactive Energy and Cloud Energy System, Dynamic Charging Systems for Vehicle Batteries and Distributed Energy Systems.